Motion artifacts in optical coherence tomography with frequency-domain ranging

S. H. Yun, G. J. Tearney, J. F. de Boer, and B. E. Bouma

Harvard Medical School and Wellman Center for Photomedicine,
Massachusetts General Hospital
50 Blossom Street, BAR-718, Boston, Massachusetts 02114
syun@hms.harvard.edu

Abstract: We describe results of theoretical and experimental investigations of artifacts that can arise in spectral-domain optical coherence tomography (SD-OCT) and optical frequency domain imaging (OFDI) as a result of sample or probe beam motion. While SD-OCT and OFDI are based on similar spectral interferometric principles, the specifics of motion effects are quite different because of distinct signal acquisition methods. These results provide an understanding of motion artifacts such as signal fading, spatial distortion and blurring, and emphasize the need for fast image acquisition in biomedical applications.

OCIS codes: (110.4500) Optical coherence tomography; (170.0110) Imaging Systems; (170.4500) Optical coherence tomography; (170.3880) Medical and biological imaging

References and links

1. N. Bankman, *Handbook of medical imaging* (Academic Press, San Diego, 2000).
2. R. J. Alfidi, W. J. MacIntyre, and . R. Haaga, "The effects of biological motion in CT resolution," Am. J. Radiol. **127**, 11-15 (1976).
3. M. L. Wood and R. M. Henkelman, "NMR image artifact from periodic motion," Med. Phys. **12**, 143-151 (1985).
4. S. K. Nadkarni, D. R. Boughner, M. Drangova, and A. Fenster, "In vitro simulation and quantification of temporal jitter artifacts in ECG-gated dynamic three-dimensional echocardiography," Ultrasound in Med. & Biol. **27**, 211-222 (2001).
5. D. Huang, E. A. Swanson, C. P. Lin, J. S. Schuman, W. G. Stinson, W. Chang, M. R. Hee, T. Flotte, K. Gregory, C. A. Puliafito, and J. G. Fujimoto, "Optical coherence tomography," Science **254**, 1178-1181 (1991).
6. J. G. Fujimoto, M. E. Brezinski, G. J. Tearney, S. A. Boppart, B. Bouma, M. R. Hee, J. F. Southern, and E. A. Swanson, "Optical biopsy and imaging using optical coherence tomography," Nat. Medicine **1**, 970-972 (1995).
7. R. C. Youngquist, S. Carr, and D. E. N. Davies, "Optical coherence-domain reflectometry: A new optical evaluation technique," Opt. Lett., **12**, 158-160 (1987).
8. A. F. Fercher, C. K. Hitzenberger, G. Kamp, and S. Y. El-Zaiat, "Measurements of intraocular distances by backscattering spectral interferometry," Opt. Comm. **117**, 43-48 (1995).
9. G. Hausler and M. W. Lindner, "Coherence radar and spectral radar - new tools for dermatological diagnosis," J. Biomed. Opt. **3**, 21-31 (1998).
10. M. Wojtkowski, T. Bajraszewski, P. Targowski, and A. Kowalczyk, "Real time in vivo imaging by high-speed spectral optical coherence tomography," Opt. Lett. **28**, 1745-1747 (2003).
11. S. H. Yun, G. J. Tearney, B. E. Bouma, B. H. Park, and J. F. de Boer, "High-speed spectral domain optical coherence tomography at 1.3 µm wavelength," Opt. Express **11**, 3598-3604 (2003), http://www.opticsexpress.org/abstract.cfm?URI=OPEX-11-26-3598
12. N. Nassif, B Cense, B. H. Park, S. H. Yun, G. J. Tearney, B. E. Bouma, T. C. Chen, and J. F. de Boer, "In vivo high-resolution video-rate spectral-domain optical coherence tomography of the human retina and optic nerve," Opt. Express **12**, 367-376 (2004), http://www.opticsexpress.org/abstract.cfm?URI=OPEX-12-3-367
13. F. Lexer, C. K. Hitzenberger, A. F. Fercher, and M. Kulhavy, "Wavelength-tuning interferometry of intraocular distances," Appl. Opt. **36**, 6548-6553 (1997).
14. S. R. Chinn, E. Swanson, and J. G. Fujimoto, "Optical coherence tomography using a frequency-tunable optical source," Opt. Lett. **22**, 340-342 (1997).

#3980 - $15.00 US Received 5 March 2004; revised 17 June 2004; accepted 21 June 2004

15. B. Golubovic, B. E. Bouma, G. J. Tearney, and J. G. Fujimoto, "Optical frequency-domain reflectometry using rapid wavelength tuning of a Cr^{4+}:forsterite laser," Opt. Lett. **22**, 1704-1706 (1997).
16. S. H. Yun, G. J. Tearney, J. F. de Boer, N. Iftimia, and B. E. Bouma, "High-speed optical frequency-domain imaging," Opt. Express **11**, 2953-2963 (2003), http://www.opticsexpress.org/abstract.cfm?URI=OPEX-11-22-2953
17. T. Mitsui, "Dynamic range of optical reflectometry with spectral interferometry," Jap. J. of App. Phys. **38**, 6133-6137 (1999).
18. R. Leitgeb, C. K. Hitzenberger, and A. F. Fercher, "Performance of Fourier domain vs. time domain optical coherence tomography," Opt. Express **11,** 889-894 (2003), http://www.opticsexpress.org/abstract.cfm?URI=OPEX-11-8-889
19. J. F. de Boer, B. Cense, B.H. Park, M. C. Pierce, G. J. Tearney, and B. E. Bouma, "Improved signal-to-noise ratio in spectral-domain compared with time-domain optical coherence tomography," Opt. Lett. **28**, 2067-2069 (2003).
20. M. A. Choma, M. V. Sarunic, C. Uang, and J. A. Izatt, "Sensitivity advantage of swept source and Fourier domain optical coherence tomography," Opt. Express **11**, 2183-2189 (2003), http://www.opticsexpress.org/abstract.cfm?URI=OPEX-11-18-2183
21. N. Nassif, B. Cense, B. H. Park, S. H. Yun, T. C. Chen, B. E. Bouma, G. J. Tearney, and J. F. de Boer, "In vivo human retinal imaging by ultrahigh-speed spectral domain optical coherence tomography," Opt. Lett. 29, 480-482 (2004).
22. W. Eickhoff and R. Ulrich, "Optical frequency domain reflectometry in single-mode fiber," App. Phy. Lett. **39**, 693-695 (1981).
23. E. Brinkmeyer and R. Ulrich, "High-resolution OCDR in dispersive waveguide," Electron. Lett. **26**, 413-414 (1990).
24. J. M. Schmitt and A. Knuttel, "Model of optical coherence tomography of heterogeneous tissue," J. Opt. Soc. Am. A **14**, 1231-1242 (1997).
25. E. A. Swanson, D. Huang, M. R. Hee, J. G. Fujimoto, C. P. Lin, and C. A. Puliafito, "High-speed optical coherence domain reflectometry," Opt. Lett. 17, 151-153 (1992).
26. J. M. Schmitt, S. H. Xiang, and K. M. Yung, "Speckle in optical coherence tomography," J. Biomed. Opt. **4**, 95-105 (1999).
27. S.-M. Stengel, Y. Allemann, M. Zimmerli, E. Lipp, N. Kucher, P. Mohacsi, and C. Seiler, "Doppler tissue imaging for assessing left ventricular diastolic dysfunction in heart transplant rejection," Heart **86**, 432-437 (2001).
28. M. V. Sivak Jr., K. Kobayashi, J. A. Izatt, A. M. Rollins, R. Ung-runyawee, A. Chak, R. C. K. Wong, G. A. Isenbert, and J. Willis, "High-resolution Endoscopic imaging of the GI tract using optical coherence tomography," Gastrointest. Endosc. **51**, 474-479 (2000).
29. G. J. Tearney, H. Yabushita, S. L. Houser, H. T. Aretz, I. K. Jang, K. Schlendorf, C. R. Kauffman, M. Shishkov, E. F. Halpern, and B. E. Bouma, "Quantification of macrophage content in atherosclerotic plaques by optical coherence tomography," Circulation **106**, 113-119 (2003)
30. G. J. Tearney, S. A. Boppart, B. E. Bouma, M. E. Brezinski, N. J. Weissman, J. F. Southern, and J. G. Fujimoto, "Scanning single-mode fiber optic catheter-endoscope for optical coherence tomography," Opt. Lett. **21**, 1-3 (1996).
31. A. E. Siegman, *Lasers* (University Science Books, Mill Valley, 1986), Chap. 9.
32. S. H. Yun, C. Boudoux, G. J. Tearney, and B. E. Bouma, "High-speed wavelength-swept semiconductor laser with a polygon-scanner-based wavelength filter," Opt. Lett. **28**, 1981-1983 (2003).

1. Introduction

Image artifacts resulting from motion have been important topics of research in nearly all medical imaging modalities because they may degrade image quality and cause inaccurate clinical interpretation of images [1-4]. Artifacts can arise when the object being imaged is moved during data acquisition but is assumed stationary in the image reconstruction process. In each imaging modality, motion artifacts can present in different forms and with different magnitudes. Understanding basic motion effects in a particular imaging method is an essential step toward the development of techniques to avoid or compensate resulting artifacts.

Optical coherence tomography (OCT) is a relatively new imaging modality using light for highly-sensitive imaging of a biological sample with high spatial resolution [5,6]. OCT was originally developed based on low coherence interferometry [7] where the time delay of optical echoes is determined using a low-coherence optical source and a delay-scanning

#3980 - $15.00 US Received 5 March 2004; revised 17 June 2004; accepted 21 June 2004

interferometer. Optical interferometric imaging methods using frequency domain ranging have recently received considerable interest due to their high image acquisition speed and sensitivity. Two frequency domain methods have been demonstrated to date: spectral-domain optical coherence tomography (SD-OCT) [8-12] and optical frequency domain imaging (OFDI) [13-16]. In SD-OCT, the spectral interference fringe is measured in the spatial domain by means of a diffraction grating and a charge-coupled device (CCD) array. In OFDI, the spectral fringe is mapped to the time domain by use of a frequency-swept light source and is measured with a photodetector as a function of time. Since each data point of the spectral fringe links to the corresponding spatial frequency component of the depth profile of the sample, the axial line of an image (A-line) is obtained by performing a discrete Fourier transform of the acquired data. Since the Fourier transform process involves integration of the entire data set obtained in a single A-line period, the signal-to-noise ratio (SNR) is enhanced relative to time domain ranging [16-21]. This improvement in SNR is particularly advantageous for applications requiring high image acquisition rates such as screening for disease and surveillance of large tissue volumes. It is, however, conceivable that the integration effect enhances the sensitivity to sample motion because the motion-induced change in signal is also integrated over the entire A-line acquisition period.

While both SD-OCT and OFDI are based on the same fundamental principle of optical interferometric imaging, the specifics of motion effects are quite different because of distinct signal acquisition methods. SD-OCT measures the interference signal in a time-integrated manner; however, OFDI obtains the signal as a function of time. In SD-OCT, for instance, a path length change in the interferometer results in phase drift in the interference fringe [18]. If the phase drifts over more than π during a single A-line acquisition, the measured amplitude of the interference fringe can be considerably diminished, resulting in a degradation of SNR. A question may also arise whether this fringe washout can occur simply by scanning a probe beam over a stationary sample if the sample has internal structures with spatially varying depths. In biological samples, the mean depth to a particular structure may change by a large number of optical wavelengths between A-lines by beam scanning. In OFDI, the signal modulation frequency is uniquely related to depth in a sample [22,23]. In terms of signal acquisition and processing, OFDI is analogous to conventional magnetic resonance imaging (MRI) [1] in which the spatial position is encoded in the spin rotation frequency by using gradient magnetic fields. Therefore, it is expected that the motion effects in OFDI may be similar to those in MRI.

In this paper, we describe the results of theoretical and experimental investigation on the motion effects in SD-OCT and OFDI. Section 2 concerns SD-OCT, and Section 3 describes OFDI. For each of the imaging methods, we describe a theoretical analysis, experimental verifications, and discussion on the implications of the motion effects in clinical applications. Section 4 summarizes the results.

2. Spectral-Domain Optical Coherence Tomography (SD-OCT)

2.1 Theory

2.1.1 Principle of operation

Figure 1 shows the basic configuration of an SD-OCT system. Broadband light is split into a sample arm and a reference arm that is terminated by a mirror at its distal end. A probe at the end of the sample arm delivers light to a sample and receives the light backscattered from within the sample. The light returned from the two interferometer arms is recombined and directed to a spectrometer consisting of a diffraction grating and a CCD array. Individual pixels of the CCD array measure the optical power as a function of wavenumber, $k = 2\pi/\lambda$ where λ is the optical wavelength. A discrete Fourier transform (DFT) of the CCD scan output produces an axial reflectance profile of the sample (A-line). A 2-D tomographic image

#3980 - $15.00 US Received 5 March 2004; revised 17 June 2004; accepted 21 June 2004

is obtained by acquiring multiple A-lines as the probe beam is scanned over the sample along a transverse direction.

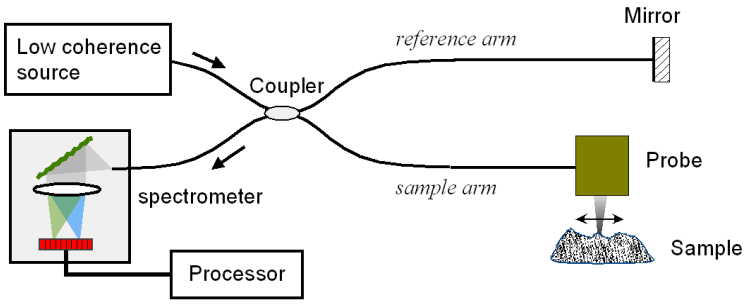

Fig. 1. Basic configuration of single-mode-fiber-based SD-OCT.

The output voltage of each CCD pixel is proportional to the number of photon-generated electrons accumulated during an exposure time, T, of the CCD. The A-line acquisition time T becomes equal to the A-line period if the CCD is operated with a 100% duty cycle. The photocurrent associated with the fringes arising from interference between the reference and sample light can be expressed as [8,24]

$$i(k) = \gamma\sqrt{S_r(k)S_s(k)}\,\mathrm{Re}\{\iiint dxdydz\; r(x,y,z)g(x-x_b, y-y_b, z-z_b)\exp[-i\,2k(z-z_b)]\}. \quad (1)$$

Here, $S_r(k)$ and $S_s(k)$ denote the spectral power density of the reference arm and sample arm light, γ is the photon-to-electron conversion efficiency, Re{} denotes the real part (neglected hereinafter for simplicity), (x, y, z) denote the coordinate of a reference frame fixed to the sample, $r(x, y, z)$ represents the complex-valued backscattering coefficient of the sample which is characterized by both local variations of the refractive index and the round-trip attenuation of light in the sample, $g(x, y, z)$ denotes the intensity profile of the probe beam normalized to $\iint g\,dx\,dy = 1$, (x_b, y_b) denote the transverse coordinates of the probe beam in the sample, and z_b denotes the longitudinal coordinate of the zero path length point of the interferometer. For a Gaussian beam with a large confocal parameter, the intensity profile is given by

$$g(x,y,z) \approx \frac{4\ln 2}{\pi w_0^{\,2}}\exp\left[-4\ln 2\,(x^2+y^2)/w_0^{\,2}\right], \quad (2)$$

where w_0 denotes the full-width-half-maximum (FWHM) of the beam profile. In Eq. (1), the explicit dependence on the intensity profile, g, rather than an electric field profile of the probe beam can be understood by considering the mode field profile of the sample arm fiber, which is by definition given by Eq. (2) at the sample location. The amplitude of the backscattered light received by the sample arm fiber is determined by an overlap integral between the scattered field and the mode field, resulting in the dependence on the intensity beam profile in Eq. (1).

Integrating the photocurrent over a duration T gives the number of electrons as

$$N(k) = \gamma\sqrt{S_r(k)S_s(k)}\int_{-T.2}^{T/2} dt \iiint dxdydz\; r(x,y,z)g(x-x_b, y-y_b)\exp[-i\,2k(z-z_b)] \quad (3)$$

A complex-valued A-line profile $F(Z)$ is obtained by a DFT of Eq. (3) with respect to $2k$:

$$F(Z) \approx \int_{-\infty}^{\infty} N(k)e^{i2kZ}\; d(2k)\;, \quad (4)$$

#3980 - $15.00 US
Received 5 March 2004; revised 17 June 2004; accepted 21 June 2004

where the approximation becomes an equality when the spectrometer measures the entire spectrum. Using $\sqrt{S_r(k)S_s(k)} = P_0 \exp[-4\ln 2(k-k_0)^2/\Delta k^2]$ where k_0 is the center wavenumber of the light source and Δk is FWHM spectral width in wavenumber, we get

$$F(Z) \propto \frac{\gamma P_0 T}{{w_0}^2 \delta z_0} \iiint dxdydz\, r(x,y,z)\, e^{i2k_0(Z-z+z_b)}\, e^{-4\ln 2\frac{(x-x_b)^2}{{w_0}^2}}\, e^{-4\ln 2\frac{(y-y_b)^2}{{w_0}^2}}\, e^{-4\ln 2\frac{(Z-z+z_b)^2}{\delta {z_0}^2}}, \quad (5)$$

where $\delta z_0 = 4\ln 2/\Delta k$ denotes the axial resolution [25]. The amplitude of $F(Z)$ is proportional to a coherent sum of all backscattered light generated from a coherence volume at $Z = z$ with a size given by the probe beam area and coherence length of the light source.

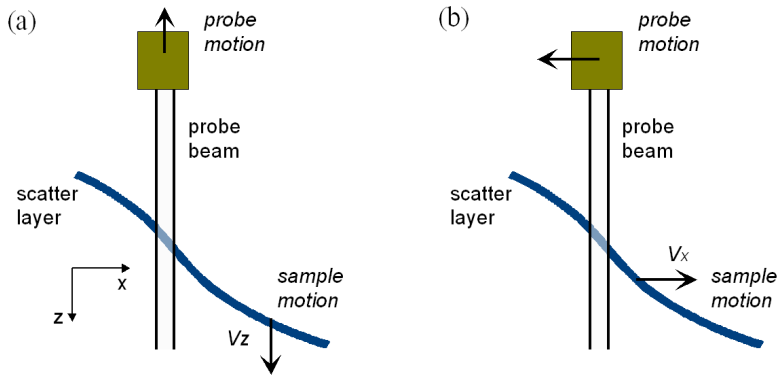

Fig. 2. Illustrations of (a) axial and (b) transverse motion of a sample (scatter layer) and probe beam.

2.1.2 Axial motion

Figure 2(a) depicts a situation where the longitudinal distance from the probe to sample is changed in time by axial motion of the sample or the probe. The effect of sample motion is identical to the effect of probe motion at the opposite velocity. Therefore, we will assume a stationary probe and consider only sample motion without loss of generality. Considering a single layer of scatterers simplifies Eq. (3) by substituting $r(x,y,z) = r(x,y)\,\delta(z - z(x,y))$. As a result of the axial motion, z_b is no longer a constant but is given by $z_b - v_z t$ where v_z denotes the axial velocity of the sample. The backscattering amplitude $r(x, y, z)$ is invariant as we assume that the scattering layer is under rigid motion. For a sample consisting of multiple internal structures moving at different velocities between each other, the analysis described here can be extended simply by applying it to individual structures separately.

Replacing z_b to $z_b - v_z t$ in Eq. (3) leads to

$$N(k) = \gamma\sqrt{S_r(k)S_s(k)} \int_{-T/2}^{T/2} dt \iint dxdy\, r(x,y)\, g(x-x_b, y-y_b) \exp\left[-i\,2k\{z(x,y) - z_b + v_z t\}\right]. \quad (6)$$

Performing the time integration, we get

$$N(k) = \gamma T\sqrt{S_r(k)S_s(k)} \iint dxdy\, r(x,y)\, g(x-x_b, y-y_b) \exp[-i\,2k(z-z_b)] \frac{\sin(k\Delta z)}{k\Delta z} \quad (7)$$

$$= N_0(k, \Delta z = 0) \frac{\sin(k\Delta z)}{k\Delta z}, \quad (8)$$

#3980 - $15.00 US
Received 5 March 2004; revised 17 June 2004; accepted 21 June 2004

where N_0 denotes the number of signal electrons obtained at v_z = 0, and $\Delta z = |v_z T|$ is the amount of axial displacement of the sample during the integration time T. Equations 7 and 8 imply two motion-induced phenomena. First, in performing the Fourier transform of Eq. (8) via. Eq. (4), the factor $\sin(k\Delta z)/(k\Delta z)$ can be approximated by a constant $\sin(k_0\Delta z)/(k_0\Delta z)$ in the case of $|\Delta z| << |z - z_b|$. Therefore, Eq. (8) asserts that the axial motion gives rise to an SNR penalty by a factor of $\sin^2(k_0\Delta z)/(k_0\Delta z)^2$. The SNR penalty can be understood in terms of the fringe washout due to the continuous phase change of fringes during the integration time. Second, when $k\Delta z >> 1$ broadening of the axial resolution arises because the Sinc function in Eq. (7) limits the effective spectral bandwidth. This effect may be described as a convolution of the original image with a rect function given by the Fourier transform of the sinc function.

2.1.3 Transverse motion

Figure 2(b) illustrates a situation where the probe and sample are moved relative to each other along a transverse coordinate, x. Without loss of generality, we will assume a stationary probe again and consider a scattering layer (sample) moving at constant velocity v_x. Replacing x_b to $x_b - v_x t$ in Eq. (3) we get

$$N_s(k) = \gamma\sqrt{S_r(k)S_s(k)}\int_{-T/2}^{T/2} dt \iint dx dy\; r(x,y)\, g(x - x_b + v_x t, y - y_b)\exp\left[-i2k\,(z - z_b)\right], \quad (9)$$

Performing the time integration leads to

$$N_s(k) = \gamma T\sqrt{S_r(k)S_s(k)}\iint dx dy\; r(x,y)\, G(x - x_b, y - y_b)\exp\left[-i\,2k(z - z_b)\right], \quad (10)$$

where

$$G(x,y) = \frac{1}{T}\int_{-T/2}^{T/2} g(x + v_x t, y)\, dt\,. \quad (11)$$

Equation (10) states that the effect of the transverse motion is merely a change of the beam profile from g to G defined in Eq. (11). $G(x, y)$ is referred to as the effective beam profile and represents the amount of beam exposure at the location (x, y). Physically, $G(x, y)$ represents an enlarged area illuminated by the probe beam during the integration time. Examples of the effective beam profile are shown in Fig. 3(a) for the Gaussian probe beam defined in Eq. (2). $G(x, y=0)$ is shown for four different values of the transverse displacement, $\Delta x = |v_x T|$, normalized to the beam size, w_0. The area of the profile is conserved i.e. $\iint G\, dx\, dy = \iint g\, dx\, dy$.

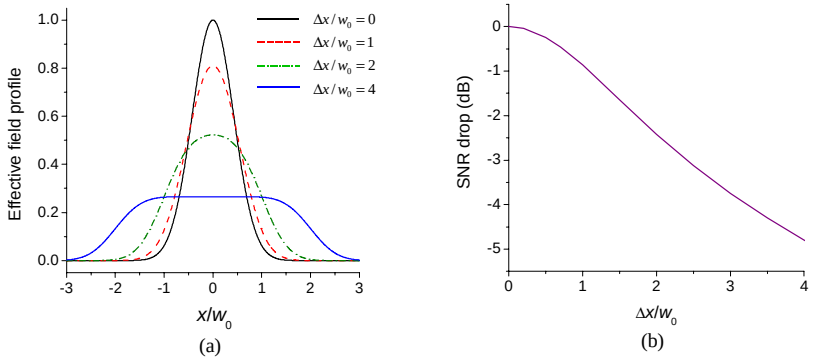

Fig. 3. (a) Effective intensity profiles of the probe beam at four different normalized displacements. (b) Mean SNR drop for a random scattering scample as a function of the normalized transverse displacement.

#3980 - $15.00 US
Received 5 March 2004; revised 17 June 2004; accepted 21 June 2004

Equation (10) implies two effects of transverse motion. One is degradation in transverse resolution. This is quite obvious from Fig. 3(a). The degradation will lead to a blurring of an image along the direction of motion. The curves in Fig. 3(a) show that the FWHM is increased by a factor of 1.25 for $\Delta x/w_0$ = 1 and 4-fold for $\Delta x/w_0$ = 4. The second effect of transverse motion is a reduction in SNR. The SNR is expected to decrease because the signal from a particular scatterer is collected during only a fraction of the time of each A-line acquisition. For a random scattering sample where signals from different scatterers are mutually uncorrelated, the speckle-averaged signal power will be proportional to $\iint G^2\, dx\, dy$. As the velocity increases, the width of the profile G increases and, therefore, the speckle-averaged signal power decreases. Figure 3(b) shows the calculated curve for the amount of SNR drop, which may be expressed as: SNR decrease (dB) $\approx -5\log(1+0.5\Delta x^2 / w_0^2)$. The actual SNR decrease of a biological sample may depend on its scattering properties such as scatterer size and distribution. For a mirror-like sample the signal power is proportional to $(\iint G\, dx\, dy)^2 = 1$ which is invariant against transverse motion. It should be noted that transverse motion does not cause the fringe washout as in axial motion because the phase of the interference fringe from each scatterer is invariant during a single A-line acquisition whereas it is chirped in the case of axial motion.

2.2. Experiments

2.2.1 SD-OCT system

Figure 4 shows a schematic of the SD-OCT system used in the experiments. The light source was a semiconductor optical amplifier producing amplified spontaneous emission (ASE) centered at 1.31 μm with a FWHM bandwidth of 66 nm and a polarized output power of 8 mW. In the sample arm, a galvanometer-mounted mirror was used for transverse beam scanning. The numerical aperture of the probe was 0.054, which resulted in a confocal parameter of 1.1 mm and a FWHM spot size of w_0 = 18 μm. The spectrometer consisted of a diffraction grating, focusing lens, and InGaAs line scan camera (LSC) with a 512-pixel CCD array. The output of the camera was digitized using a 12-bit data acquisition board (DAQ). The acquired data were interpolated to correct for nonlinearity in k-space and processed via a DFT to produce images. The camera was operated at a readout rate of 18.94 kHz with an integration time of 24.4 μs (46% duty cycle). The sensitivity of the SD-OCT system was measured to be greater than 105 dB over a depth range of 2 mm. The free-space axial resolution was measured to be between 12 and 14 μm FWHM over the depth range of 2 mm. The operating conditions and performance of the system are described in detail in Ref. 11.

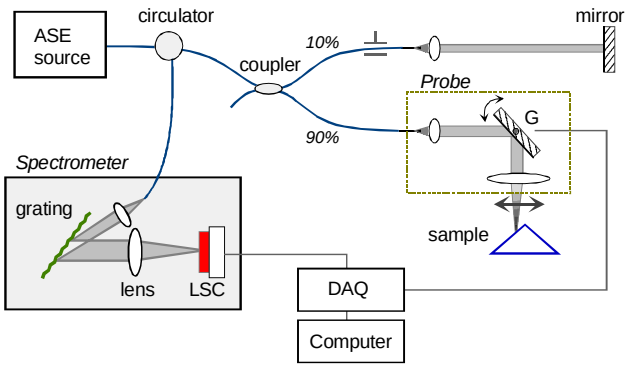

Fig. 4. Schematic of the experimental SD-OCT system. ASE; amplified spontaneous emission, G: galvanometer, LSC; line scan camera, DAQ; data acquisition board.

#3980 - $15.00 US
Received 5 March 2004; revised 17 June 2004; accepted 21 June 2004

2.2.2 Axially moving mirror

To investigate the effect of axial motion, we measured A-line profiles from a mirror mounted on an oscillating loud speaker. A neutral-density filter was used to lower the total reflectivity from the mirror to −55 dB. For this experiment, the galvanometer in the probe was not driven and was fixed to its neutral position. The axial position of the mirror at zero voltage applied to the speaker coincided with the focal plane of imaging lens. Figure 5(a) shows the image of 500 consecutive A-lines obtained when the speaker was driven with a sinusoidal waveform with peak-to-peak vibration amplitude of 1.76 mm at a frequency of 40 Hz. The horizontal axis represents the time (total 26.4 ms) or A-line number (1 to 500). The vertical axis of the image consists of 256 pixels and extends over a depth of 2.08 mm. The image was plotted with a logarithmic inverse grayscale over a reflectivity range of 35 dB. The peak signal power of each A-line profile is plotted in Fig. 5(b) as a solid line (black). The dashed line (brown) denotes the theoretical curve of $\sin^2(k_0\Delta z)/(k_0\Delta z)^2$ where Δz was calculated by assuming a perfect sinusoidal oscillation of the speaker with the measured amplitude of 1.76 mm and frequency of 40 Hz. The theoretical curve agrees well with the experimental results. Harmonic distortion in the speaker motion and a depth-dependent reflectivity of the mirror due to finite confocal parameter of the probe beam may account for the slight offset in the peak positions and dissimilar peak values compared to the experimental curve. Figures 5(c) and (d) show the results of a similar experiment conducted for a mirror displacement amplitude of 0.22 mm and frequency of 80 Hz.

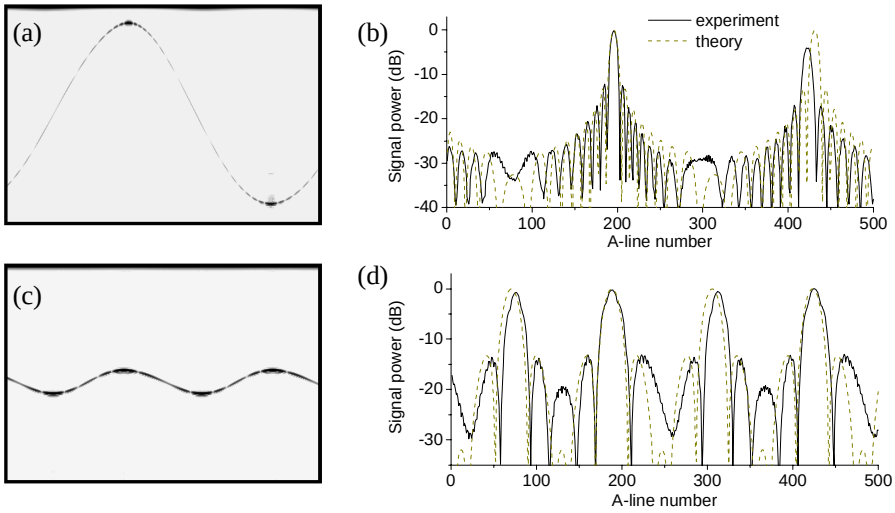

Fig. 5. (a) An SD-OCT image (500 A-lines) of a mirror vibrating at a peak-to-peak amplitude of 1.76 mm and frequency of 40 Hz. (b) Maximum signal power measured (solid line, black) and calculated theoretically (dashed line, brown). (c) An image of a mirror moving at an amplitude 0.22 mm and frequency of 80 Hz. (d) Signal power measured (solid line, black) and calculated theoretically (dashed line, brown).

2.2.3 Transverse beam scanning

The effect of transverse motion was investigated by scanning the probe beam over a sample. In this experiment, the speaker driven mirror was replaced with a 90-degree BK7 prism with its surfaces roughened by using a polishing film with a 15 μm grain size. The arrangement of the sample and the probe beam is depicted in Fig. 4. The galvanometer was driven with a saw-tooth waveform at a frequency of approximately 38 Hz in synchrony with the camera read out.

#3980 - $15.00 US
Received 5 March 2004; revised 17 June 2004; accepted 21 June 2004

To obtain various scan speeds, the peak-to-peak amplitude of the galvanometer voltage was varied from 0 to 20 V. At amplitudes greater than 5 V, the scan distance was limited by the finite size of the lens and the maximum angular scan range of the galvanometer. However, the scan speed in the middle of the scan range, near its neutral position, was linearly proportional to the voltage swing with a coefficient of ~110 mm/V. During a single galvanometer scan period (26.4 ms), 500 A-lines were acquired at a rate of 18.94 kHz.

Figure 6 depicts images of the prism obtained at different galvanometer drive voltages. The image was plotted in a logarithmic inverse grayscale over a reflectivity range of 20 dB. The vertical axes contain 256 pixels and extend over a depth of 2.08 mm. The scale bars represent 1.0 mm. The shift of the probe beam between adjacent A-lines is proportional to the voltage amplitude with a coefficient of ~7.6 μm/V. Therefore, the images obtained at higher amplitudes consist of fewer A-lines. Because the camera had a 46% duty cycle, the normalized transverse displacement is $\Delta x/w_0 = 0.19$ [V^{-1}]. Images obtained at 10 and 20 V exhibit significant blurring particularly along the transverse direction and exhibit disconnected surface lines.

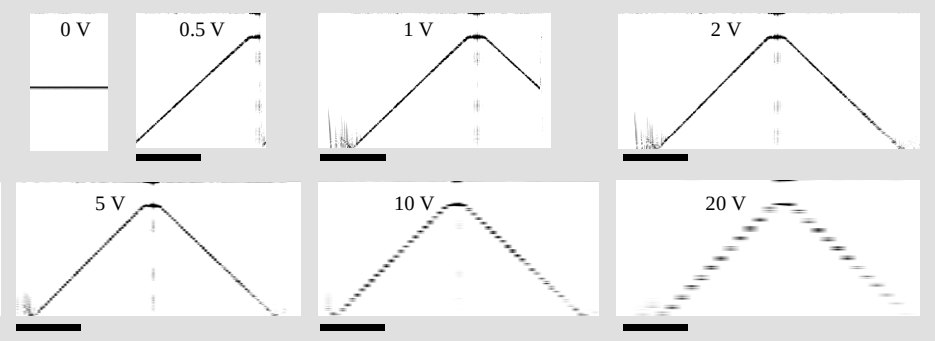

Fig. 6. SD-OCT images of a 90-degree prism at various amplitudes of the galvanometer scan voltage. With increasing amplitude, the scan velocity is increased and therefore the image contains fewer A-lines. The scale bars represent 1.0 mm.

To compare the measurements of Fig. 6 with the theory described in Section 2.1.3, the signal power and FWHM of 10 A-lines at the slope of the prism near the center of the images were analyzed. Due to speckle [26], the 10 A-line profiles in each image had variations in signal peak power with a standard deviation of +/- 3 dB. Figure 7(a) shows the mean value of the 10 measured values (circles) as a function of the normalized displacement between adjacent A-lines. The measurements agree well with the theoretical expectation (red line, Fig. 7a). Figure 7(b) also shows the minimum FWHM measured from the 10 A-line reflectance profiles (circles). The result seems to indicate that there is apparently no degradation in axial resolution up to $\Delta x/w_0 = 4$. One may anticipate that the FWHM should increase with increasing $\Delta x/w_0$ simply because the probe beam moves over a slanted surface. However, because our sample had a relatively large scatterer size of approximately 15 μm, only a few to several scatterers might be illuminated during a single A-line acquisition at $\Delta x/w_0$ up to 4. Apparently in the A-line with the minimum FWHM, a single scatterer generated a dominant signal over the others. In this case, the FWHM would be expected to have a value similar to the intrinsic axial resolution of the SD-OCT system. The flat line (blue) at 13 μm represents the mean axial resolution of the system measured with a stationary mirror sample.

#3980 - $15.00 US Received 5 March 2004; revised 17 June 2004; accepted 21 June 2004

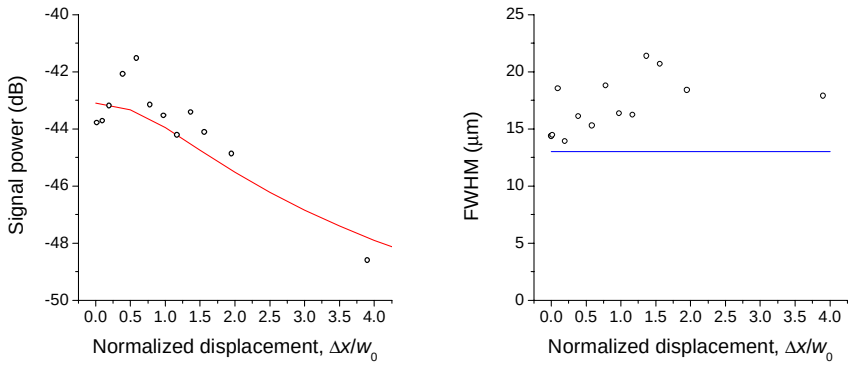

Fig. 7. (a) Signal peak power (open circles, black) measured from the average of 10 A-line profiles for each normalized displacement. Red line: theorical fit curve for speckle-averaged signal power. (b) Minimum FWHM of the image (open circles, black) obtained from 10 A-line amplitude profiles. Blue line: theoretical curve for axial resolution expected from a mirror sample.

To investigate the effect of beam scanning for a biological sample, we imaged the ventral portion of a volunteer's finger near a skin fold. Figure 8 depicts the image (256 axial × 500 transverse pixels) acquired at an A-line acquisition rate of 18.94 kHz. The focal point of the imaging lens was positioned in the middle of the depth range. The vertical axis extends over a depth of 2.08 mm. The horizontal axis extends over a distance of 5.0 mm. The shift of the probe beam between adjacent A-lines was approximately 10 μm. With the 46% duty cycle, this corresponds to $\Delta x/w_0 = 0.25$. At this low value, the previous results in Fig. 7 predict that the SNR decrease and resolution broadening should be negligible. Indeed, no signature of such degradation is seen in Fig. 8. The skin fold region with steep structural lines appears as sharp as other areas, despite a depth change by several hundreds optical wavelengths during a single A-line acquisition time.

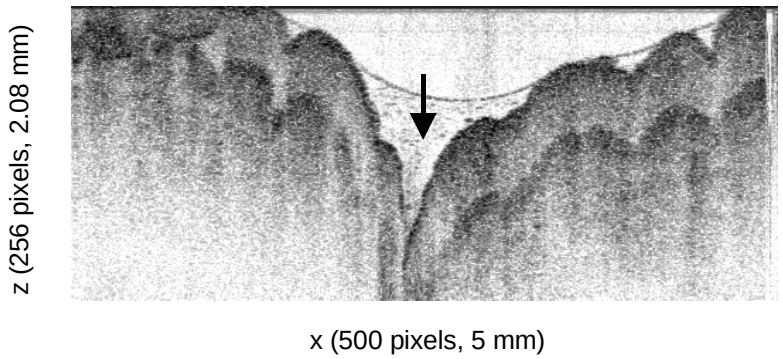

Fig. 8. SD-OCT image of a human finger (256 axial × 500 transverse pixels, 2.08 mm × 5 mm) obtained at an A-line rate of 19 kHz. The arrow indicates a skin fold region.

2.3 Discussion

We have demonstrated that the axial motion of a sample relative to the probe beam in SD-OCT results in SNR degradation due to fringe washout. Transverse sample motion or transverse beam scanning does not cause fringe washout, but results in degradation in transverse resolution and SNR.

#3980 - $15.00 US
Received 5 March 2004; revised 17 June 2004; accepted 21 June 2004

Motion effects can arise from various sources in medical imaging *in vivo*. The main causes include patient motion, physiological phenomena such as cardiac motion, blood flow, pulsation, and catheter movement associated with beam scanning or uncontrolled movement of operator's hand. Furthermore, environmental changes such as mechanical vibration, sound waves, and temperature drift can alter the path length difference in the interferometer, resulting in SNR degradation through fringe washout. The SNR penalty from fringe washout is given by $\sin^2(k_0\Delta z)/(k_0\Delta z)^2$. An SNR margin of 10 dB limits Δz to be less than 0.37 λ_0. This is equal to 0.48 μm for λ_0 = 1.3 μm and corresponds to 19.7 mm/s in velocity for T = 24.4 μs. This value may be large enough so that the effect of typical environmental changes or slow patient motion is negligible. However, fast physiological motions such as the cardiac motion in cardiovascular imaging may cause a significant SNR penalty. The maximum velocity of heart motion can be as high as 100 mm/s [27]. In the case when the sample motion causes unacceptable SNR degradation, an active method to compensate for the motion by changing the length in the interferometer arm may be required.

For many non-ophthalmic imaging applications *in vivo* [28,29], a rotating fiber-optic catheter has been used to obtain radius-circumferential images [30]. In this case, the dominant transverse motion results from the scanning of the probe beam across the lumen while the catheter rotates. To avoid excessive transverse blurring the maximum allowable transverse displacement may be set to $\Delta x/w_0$ = 1. For the SD-OCT system used in this study, the parameters w_0 = 18 μm, T = 24.4 μs, and 46 % duty cycle require that the shift of the probe beam during the A-line period should be less than 39 μm. This requirement puts a limit on the minimum number of A-lines that need to be acquired per image during one revolution of the catheter. A ranging depth of 4 mm requires a minimum of 644 A-lines per image.

3. Optical Frequency Domain Imaging (OFDI)

3.1 Theory

3.1.1 Principle of operation

Figure 9 shows a basic configuration for OFDI. The center wavelength of the tunable light source is swept continuously and repeatedly over a desired broad wavelength range. The output of the swept source is split into two paths, illuminating a stationary reference mirror and a sample. Light returning from the mirror and sample is recombined and the resulting interference is registered by a photodetector. The output of the photodetector can be digitized for analysis using an analog-to-digital converter. A discrete Fourier transform (DFT) of the sampled data obtained in each tuning period of the source is performed in a computer to produce axial reflectance profile of the sample (A-line). 2-D tomographic images are obtained by acquiring multiple A-lines consecutively as the probe beam is scanned over the sample along a transverse direction.

Let us first consider the case where the output wavenumber is tuned linearly in time i.e. $k(t) = k_0 + k_1 t$, where $k = 2\pi/\lambda$ is the wavenumber, λ is the optical wavelength, t is the time spanning from $-T/2$ to $T/2$, and T is the tuning period or equivalently A-line period. Further we assume a Gaussian tuning envelope given by

$$P_{out}(t) = P_0 \exp[-4\ln 2\, t^2/(\sigma T)^2], \tag{12}$$

where $P_{out}(t)$ denotes the output power of the source and σT the full width at half maximum (FWHM) of the tuning envelope. Equation (12) also describes the Gaussian spectral envelope of the source, where $\sigma k_1 T$ corresponds to the FWHM tuning range in wavenumber.

#3980 - $15.00 US Received 5 March 2004; revised 17 June 2004; accepted 21 June 2004

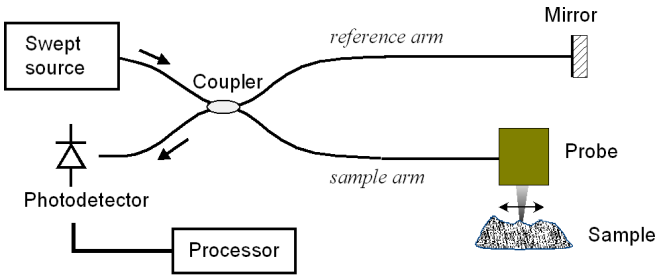

Fig. 9. Schematic of single-mode-fiber-based OFDI.

As in Section 2.1.1, let $r(x, y, z)$ denote the backscattering amplitude of the sample at the point (x, y, z) in a reference frame fixed to the sample characterized by refractive index variations and roundtrip attenuation by absorption and scattering. For a singly reflected sample, the photocurrent generated from the interference between the reference and sample light can be expressed as

$$i(t) = \gamma\sqrt{P_r(t)P_s(t)}\ \mathrm{Re}\{\iiint dxdydz\ r(x,y,z)g(x-x_b, y-y_b)\, e^{-i2k(t)(z-z_b)}\}. \quad (13)$$

Here, $P_r(t)$ denotes the optical power returned from the reference arm, $P_s(t)$ the optical power returned from the sample arm when a sample with 100% reflection is used, γ is the photon-to-electron conversion efficiency, The real-part operator, Re{}, will be neglected hereinafter for simplicity, (x_b, y_b, z_b) denotes the coordinates of the probe beam at zero path length difference of the interferometer, and $g(x, y, z)$ is the normalized intensity profile of the probe beam [Eq. (2)].

A Fourier transform of Eq. (13) with respect to $\kappa = 2k_1 t$ yields a complex-valued depth profile (A-line):

$$F(Z) = \int_{-k_1 T}^{k_1 T} i(\kappa) e^{i\kappa Z}\ d\kappa. \quad (14)$$

Assuming $\sqrt{P_r(t)P_s(t)} = P_0 \exp[-(4\ln 2)t^2/\sigma^2 T^2]$ and $\sigma^2 < 1$, we can approximate the range of the integral to $[-\infty, \infty]$, which results in

$$F(Z) \approx \gamma P_0 \iiint dxdydz\ r(x,y,z)\, g(x-x_b, y-y_b) e^{-i2k_0(z-z_b)} \int_{-\infty}^{\infty} e^{-4\ln 2\frac{\kappa^2}{(2k_1T\sigma)^2}} e^{i\kappa(Z+z_b-z)} d\kappa. \quad (15)$$

Thus,

$$F(Z) \propto \frac{\gamma P_0}{{w_0}^2 \delta z_0} \iiint dxdydz\ r(x,y,z) e^{-i2k_0(z-z_b)} e^{-4\ln 2\frac{(x-x_b)^2}{{w_0}^2}} e^{-4\ln 2\frac{(y-y_b)^2}{{w_0}^2}} e^{-4\ln 2\frac{\{Z+z_b-z(x,y)\}^2}{\delta {z_0}^2}}, \quad (16)$$

where $\delta z_0 = 4\ln 2/(k_1 T\sigma)$ denotes the FWHM axial resolution neglecting the effect of truncation of a Gaussian spectrum. Equation (17) states that the amplitude of $F(Z)$ is proportional to a coherent sum of all backscattered light from a coherence volume that has a size $w_0 \times w_0 \times \delta z_0$ and is located at a depth Z in the sample.

3.1.2 Axial motion

Figure 2(a) depicts a situation with an axially moving sample and probe. The interference signal is solely dependent on the relative motion between the scatterer and the probe beam; sample motion is identical to probe motion with the opposite velocity. Therefore, we will

#3980 - $15.00 US
Received 5 March 2004; revised 17 June 2004; accepted 21 June 2004

assume a stationary probe and consider a sample moving at a uniform velocity without loss of generality.

The signal in the presence of axial motion can be obtained by substituting $z_b(t) = z - z_0 - v_z t$ into Eq. (13) where $z_0 = z - z_b(0)$ denotes the mean path length difference, and v_z the axial velocity of the sample. The depth profile is obtained via the Fourier transform:

$$F(Z) \approx \gamma P_0 \iiint dx\,dy\,dz\, r(x,y,z)\, g(x-x_b, y-y_b)\, e^{-i2k_0 Z} \int_{-\infty}^{\infty} e^{-4\ln 2 \frac{\kappa^2}{(2k_1 T\sigma)^2}} e^{i(2k_0+\kappa)(Z-z_0-\frac{v_z}{2k_1}\kappa)}\, d\kappa \tag{17}$$

$$\propto \frac{\gamma P_0}{{w_0}^2 \delta z} \iiint dx\,dy\,dz\; r(x,y,z)\, e^{-i2k_0 z_0}\, e^{-4\ln 2 \frac{(x-x_b)^2}{{w_0}^2}}\, e^{-4\ln 2 \frac{(y-y_b)^2}{{w_0}^2}}\, e^{-4\ln 2 \frac{\{Z-[z_0+(k_0/k_1 T)\Delta z]\}^2}{\delta {z_0}^2 (1+4\sigma^2 \Delta z^2/\delta {z_0}^2)}} \tag{18}$$

where $\Delta z = v_z T$ denotes the axial displacement of the sample during a single A-line acquisition time. Equation (18) illustrates two effects of axial motion. First, the depth in the image is given by

$$Z = z_0 + z_D\,, \tag{19}$$

where

$$z_D \equiv \frac{k_0}{k_1 T}\Delta z = \frac{\pi\sigma}{2\ln 2}\frac{\delta z_0}{\lambda}\Delta z\,. \tag{20}$$

The axial shift, z_D, originates from the Doppler frequency shift generated by the moving sample. A moving sample would create a signal modulation even in the absence of tuning with the Doppler frequency given by kv_z/π. For wavelength-swept light, the Doppler frequency is added to the original modulation frequency of the OFDI signal, resulting in an erroneous depth offset. Typical values for σ and $\delta z_0/\lambda$ may be 0.5 – 0.8 and 4 – 12, respectively. Therefore, the Doppler error could be 5 to 22 times the actual displacement Δz. The second effect is broadening in axial resolution, given by

$$\frac{\delta z}{\delta z_0} = \sqrt{1 + 4\sigma^2 \frac{\Delta z^2}{\delta {z_0}^2}}\,. \tag{21}$$

The broadening arises due to signal chirping represented by the κ^2 term in the phase in Eq. (17). Even a modest displacement equal to the unperturbed axial resolution, i.e. $\Delta z = \delta z_0$, could result in a 70% broadening for $\sigma = 0.71$.

3.1.3 Transverse motion

Figure 2(b) illustrates a situation where the probe and sample are moved relative to each other along a transverse coordinate, x. Without loss of generality, we will assume a stationary probe again and consider a scattering layer (sample) moving at constant velocity v_x. Substituting $x_b(t) = x_b - v_x t$ in Eq. (13), we get

$$i(t) = \gamma\sqrt{P_r(t)P_s(t)} \iiint dx\,dy\,dz\; r(x,y,z)\, g(x - x_b + \frac{\Delta x}{T}t, y - y_b)\, e^{-i2k_0 z_0}\, e^{-i2k_1 t z_0}\,, \tag{22}$$

where $\Delta x = v_x T$ denotes the transverse displacement of the sample during the acquisition of a single A-line. Performing a Fourier transform, we get

#3980 - $15.00 US Received 5 March 2004; revised 17 June 2004; accepted 21 June 2004

$$F(Z)=\frac{\gamma P_0}{{w_0}^2}\iiint dxdydz\; r(x,y,z)e^{-i2k_0z_0}e^{-4\ln 2\frac{(y-y_b)^2}{{w_0}^2}}\int_{-k_1T}^{k_1T}e^{-4\ln 2\frac{\kappa^2}{(2k_1T\sigma)^2}}e^{-4\ln 2\frac{(x-x_b+\frac{\Delta x}{2k_1T}\kappa)^2}{{w_0}^2}}e^{i\kappa(Z-z_0)}\,d\kappa, \tag{23}$$

For a scattering sample, the integral over κ can find an approximate solution which yields

$$F(Z)\propto\frac{\gamma P_0}{w_0w_x\delta z_0}\iiint dxdydz\; r(x,y,z)e^{-i2k_0z_0}\,e^{-4\ln 2\frac{(y-y_b)^2}{{w_0}^2}}e^{-4\ln 2\frac{(x-x_b)^2}{{w_x}^2}}e^{-4\ln 2\frac{(Z-z_0)^2}{\delta z^2}}, \tag{24}$$

where

$$\frac{w_x}{w_0}=\frac{\delta z}{\delta z_0}=\sqrt{1+\sigma^2\frac{\Delta x^2}{{w_0}^2}}\,. \tag{25}$$

This equation describes a broadening of the axial and transverse resolution due to transverse motion. Figure 10(a) shows a plot of the broadening factor as a function of normalized displacement $\Delta x/w_0$ for σ = 0.71. The broadening in transverse resolution is obvious because the effective size of the probe beam is increased by the transverse motion. The broadening in axial resolution occurs because the spectral width that each scattering point on the sample experiences during a single A-line acquisition is reduced as a result of the transverse motion. For a mirror-like sample, represented by $r(x,y,z)=r_0\delta(z)$, Eq. (23) can be readily solved by performing the space integration first to show that both transverse and axial resolution are invariant as anticipated since the beam scanning over a mirror does not alter the signal. Equations (24) and (25) are valid for a random scattering sample.

Equation (24) also describes the effect of the transverse motion in signal-to-noise ratio (SNR). The SNR is influenced by the transverse motion because a larger number of scatterers are illuminated with motion, but the signal from each scatterer is collected by only a fraction of the duration of each A-line acquisition. Here we define the SNR as a ratio $|F_s(z)|^2/|F_n(z)|^2$ where $F_s(z)$ and $F_n(z)$ denote the signal and noise components, respectively, obtained from a DFT of signal and noise photocurrents via Eq. (14). The change in SNR by motion depends on the specific type of a sample. For a mirror-like sample, SNR is invariant since the transverse motion does not alter the signal and noise, as can be derived from Eq. (23). For a single point scatterer sample expressed as $r(x,y,z)=r_0\,\delta(x)\delta(y)\delta(z)$, it can be shown from Eq. (24) that the SNR decrease is given by $(1+\sigma^2\Delta x^2/{w_0}^2)^{-1}$. For a bulk random scattering medium which leads to a fully-developed speckle [26], the speckle-averaged signal power is given as an incoherent sum of signal powers from individual scatters. Assuming a homogenous scattering coefficient, it can be shown from Eq. (24) that the mean signal power is proportional to $1/({w_0}^2\delta z)^2\iiint e^{-8\ln 2\frac{(x-x_b)^2}{{w_x}^2}}e^{-8\ln 2\frac{(y-y_b)^2}{{w_0}^2}}e^{-8\ln 2\frac{(Z-z_0)^2}{\delta z^2}}dxdydz$ which is invariant against the transverse motion. On the other hand, for a 2-dimensional scattering layer oriented in the *x-y* or *y-z* plane, the SNR is given by $(1+\sigma^2\Delta x^2/{w_0}^2)^{-0.5}$. The scattering property of actual biological sample may vary between a point scatterer and bulk homogenous random scattering medium. Therefore, we may expect that the SNR decrease for a biological sample may be given by

$$SNR\ decrease\ \approx\ (1+\sigma^2\frac{\Delta x^2}{{w_0}^2})^{-\alpha}, \tag{26}$$

#3980 - $15.00 US
Received 5 March 2004; revised 17 June 2004; accepted 21 June 2004

where α ranges from 0 to 1 depending on the sample. Figure 10(b) depicts the SNR decrease for three different α values.

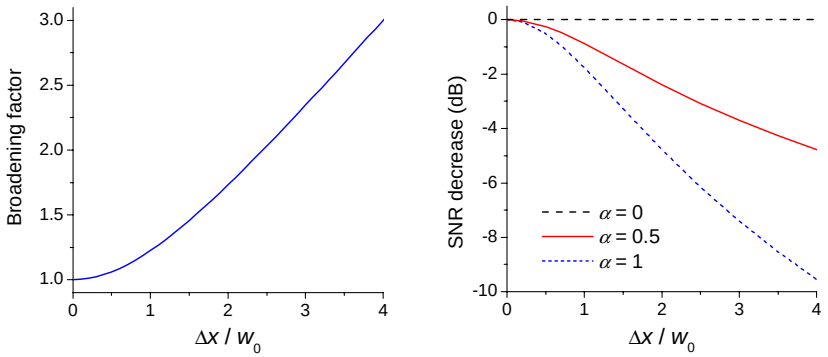

Fig. 10. (a) The magnitude of broadening in axial and transverse resolution and (b) SNR decrease arising from transverse motion as a function of normalized displacement $\Delta x / w$ for $\sigma^2 = 0.5$.

As defined in Eq. (12), σT is equal to the FWHM width of optical intensity profile and, therefore, can be interpreted as an effective integration time of the signal. This accounts for the appearance of σ in Eqs. (20), (21), (25) and (26) since Δz and Δx were defined as total displacements integrated over the entire A-line acquisition time of T rather than σT.

3.1.4 Nonlinear tuning slope

In general, the tuning of a swept source is not always linear in *k*-space. In this case, the wavenumber can be expressed as a Taylor series of time i.e. $k(t) = \sum k_m t^m$ where m = 0, 1, 2… It is well known that nonlinear sampling in *k*-space gives rise to a poor spatial resolution [23]. To avoid this problem, the detector output may be sampled with non-uniform time intervals so as to produce uniform sampling in *k*-space. Alternatively, the detector output may be sampled with a uniform time interval, and subsequently the acquired data is re-sampled by interpolation to a uniform spacing in *k*-space. This method is commonly implemented in practice. Mathematically, both methods are equivalent to a coordinate transform from t to a normalized time variable τ, defined as:

$$t = T\tau - (k_2 / k_1)T^2\tau^2 + [2(k_2 / k_1)^2 - (k_3 / k_1)]T^3\tau^3 + \cdots, \tag{27}$$

where τ spans from –0.5 to 0.5 for a single A-line acquisition. The wavenumber function then becomes linear in τ, i.e. $k(\tau) = k_0 + k_1 T\tau$. The depth profile is readily obtained with transform limited spatial resolution by a Fourier transform with respect to $\kappa = k_1 T\tau$.

Let us consider an axially moving sample described as $z_b(t) = z - \sum z_m t^m$ where $z_0 = z - z_b(0)$ denotes the mean path length difference, $z_1 = v_z$ the velocity, and z_2 the acceleration. Using Eq. (27), we get

$$i(\xi) = \gamma\sqrt{P_r(\tau)P_s(\tau)} \iiint dxdydz\, r(x,y,z)\, g(x - x_b, y - y_b) \exp[-i\sum \omega_m \tau^m], \tag{28}$$

where

$$\omega_0 = 2k_0 z_0, \quad \omega_1 = 2(k_1 z_0 + k_0 z_1)T, \quad \omega_2 = 2\{k_1 z_1 - (k_0 k_2 / k_1)z_1 + k_0 z_2\}T^2. \tag{29}$$

Here, ω_0 is a constant phase term. ω_1 corresponds to the signal frequency in τ and is responsible for the Doppler shift in Eq. (19). ω_2 represents quadratic signal chirping and

#3980 - $15.00 US
Received 5 March 2004; revised 17 June 2004; accepted 21 June 2004

therefore results in broadening of the axial resolution. The coefficient of the cubic term, ω_3 plays a similar role to third-order chromatic dispersion, leading to asymmetry of the point spread function [31].

It can be shown that the axial resolution is given by

$$\frac{\delta z}{\delta z_0} = \sqrt{1 + \frac{\sigma^4 \omega_2^2}{(4 \ln 2)^2}} \,. \tag{30}$$

This leads to Eq. (21) for the special case of linear-k tuning and linear motion. For linear-λ tuning (linearly varying output wavelength in time), the axial resolution is found to be independent of z_1; a pure linear motion does not affect the axial resolution in this special case.

3.2 Experiments

3.2.1 OFDI system

Figure 11 depicts a schematic of our OFDI system. The light source was a wavelength-swept laser comprised of a semiconductor optical amplifier and polygon-scanner-based wavelength filter in a fiber-optic cavity [32]. The tuning range of the laser was 74 nm centered at a wavelength of 1.32 μm with $\sigma = \sim 0.71$. The tuning repetition rate could be varied by controlling the polygon rotation speed from <1 kHz up to 15.7 kHz. The tuning coefficients of the laser were measured using an unbalanced Michelson interferometer. The measured values were: $k_0 = 4.76 \times 10^6$ m^{-1}, $k_1 T / k_0 = -0.051$, $k_2 T / k_1 = -0.128$, and $k_3 T^2 / k_1 = -0.075$.

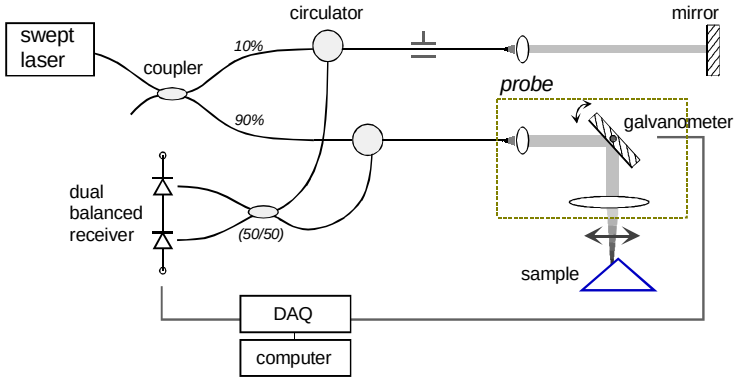

Fig. 11. Experimental setup of the OFDI system.

The probe consisted of a fiber-optic collimator, galvanometer-mounted mirror, and imaging lens. The galvanometer was driven with a saw-tooth waveform to provide a linear transverse beam scan over the sample. The numerical aperture of the probe was 0.054, which resulted in a confocal parameter of 1.1 mm and a FWHM spot size of w_0 = 18 μm. The light returned from the reference mirror and the sample was combined at a 50/50 coupler. The interference signal was measured with a dual balanced InGaAs photodetector followed by a differential transimpedance amplifier and a low pass electronic filter with a cutoff at 5 MHz. A total of 600 samples were acquired during each wavelength sweep with 94% duty cycle using a 12-bit data acquisition board. Therefore, the A-line acquisition time, T, was nearly equal to the tuning period. The acquired data was interpolated to correct for nonlinearity in k-space before DFT processing to create an image. At the maximum tuning repetition rate of 15.7 kHz, the sensitivity of the OFDI system was measured to be approximately 110 dB over the entire depth range of 3.8 mm. Details of the system is described in Ref. 16.

#3980 - $15.00 US
Received 5 March 2004; revised 17 June 2004; accepted 21 June 2004

3.2.2 Moving mirror

To investigate the effect of axial motion, we performed an experiment using a moving mirror as in Section 2.2.2. The mirror was mounted on an oscillating loud speaker were acquired. A neutral-density filter was used to lower the total reflectivity from the mirror to −55 dB. For this experiment, the probe beam was not scanned in the transverse direction but held fixed at the center of the imaging lens. The axial position of the sample mirror at zero applied voltage to the speaker coincided with the focal plane of imaging lens. Images were taken when the speaker was driven with a sinusoidal voltage waveform producing a peak-to-peak vibration amplitude of 0.78 mm at a frequency of 30 Hz.

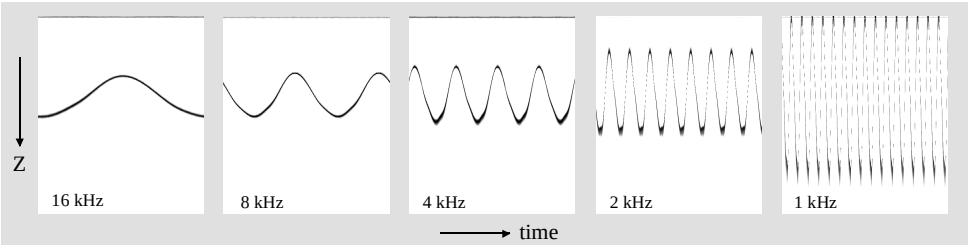

Fig. 12. OFDI images of a moving mirror (amplitude: 0.78 mm, frequency: 30 Hz) acquired at A-line rates of 16, 8, 4, 2, and 1 kHz, respectively. The vertical axis represents the depth over 3.8 mm. The horizontal axis represents the time over 520 A-line acquisition periods. The vibration amplitude in the images is artifactually increased with increasing amount as the A-line acquisition rate decreases by Doppler shift

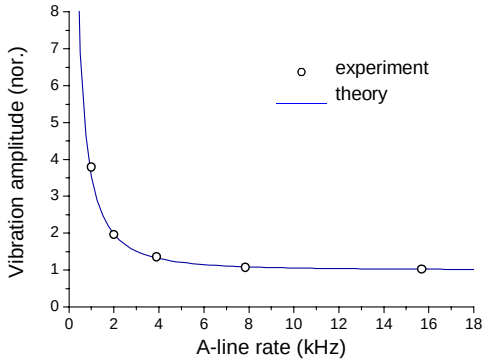

Fig. 13. Normalized amplitude of mirror motion measured from the images of Fig. 12 (circles) and predicted theoretically (line).

Figure 12 shows five images of the moving mirror obtained at five different A-line acquisition rates: 1, 2, 4, 8, and 16 kHz. For these measurements, the sampling rate of the data acquisition board was adjusted accordingly to maintain the duty cycle of data acquisition between 92 and 96%. The images are plotted in a logarithmic inverse grayscale over a reflectivity range of 20 dB. Each image consists of 520 A-lines obtained consecutively. The vertical axis of each image consists of 300 pixels and extends over a depth of 3.8 mm. The horizontal axis consists of 520 pixels and represents time or the A-line number from 1 to 520. The number of oscillation cycles in the images increases from 1 to 16 as the A-line rate is decreased. As the A-line rate is decreased, it is notable that the amplitude of the oscillation in the image is artifactually increased; the actual vibration amplitude of the mirror was kept constant. The oscillation amplitudes measured from the images are plotted in Fig. 13 (circles) after normalizing them to the value measured at an A-line rate of 16 kHz. For a sinusoidal

#3980 - $15.00 US Received 5 March 2004; revised 17 June 2004; accepted 21 June 2004

motion with a frequency f_m, Eq. (20) predicts that the amplitude in the image, normalized to the actual oscillation amplitude, is given by $[1+(2\pi f_m k_0 / k_1)^2]^{1/2}$, where f_m = 30 Hz in the experiment. The theoretical curve is shown in Fig. 13 as a solid line, and agrees well with the experimental values.

To further analyze the data, 16 A-line profiles were taken from the image acquired at an A-line rate of 2 kHz. Figure 14(a) shows the 16 representative A-line profiles, labeled 1 to 16, extracted with a uniform time interval during a single period of sample mirror oscillation. Individual A-line profiles were offset vertically for easier comparison. As a reference, the A-line profile obtained with zero voltage applied to the speaker is shown (label 0). Compared to the reference A-line, the curves 1 to 16 exhibit three distinctive differences: decreased peak value, axial broadening, and asymmetric shape. The degrees of broadening and asymmetric tilt are seen to be dependent upon the location of the mirror. Based on the theoretical formalism described in Section 3.1, we performed a numerical simulation for comparison with these measurements. The measured tuning parameters of the laser source were used up to the cubic coefficient k_3. The results of the simulation are presented in Fig. 14(b). The profile labeled 0 is a reference profile calculated assuming a stationary mirror. Curves labeled 1 to 16 depict A-line profiles predicted for an oscillating sample mirror with a vibration amplitude of 0.78 mm. The A-line profiles obtained by the simulation show similar features to those in Fig. 14(a), reproducing the oscillation with similar peak-to-peak amplitude and degree of asymmetric broadening. Curve 17 depicts the position of the moving mirror assumed in the simulation (open circles and solid line, green). It is clearly seen that the oscillation amplitude in the image was exaggerated by a factor of approximately 2 due to the Doppler shift. Additionally, there is a phase shift between curve 17 and the peaks of the A-lines. This shift arises from the velocity dependence of the Doppler shift.

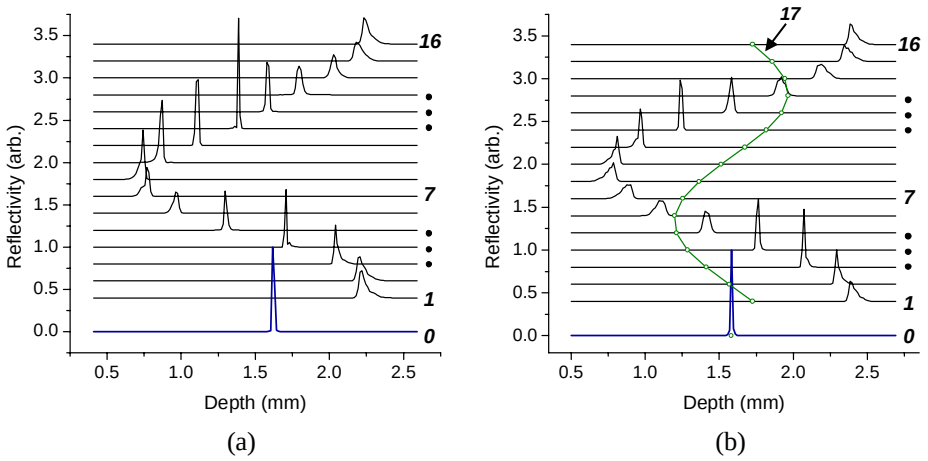

Fig. 14. (a) Measured A-line profiles (curves 1 to 16, black) obtained at an A-line rate of 2 kHz during a single cycle of sample mirror oscillation. The A-line profile obtained with a stationary mirror at its neutral position is also shown as a reference (curve 0, blue). (b) Simulation results. Curve labeled 17 (green) depicts the trace of actual mirror motion used in the simulation.

Figure 15(a) shows the axial resolution measured from A-lines 1 through 16 in Fig. 14(a) (2 kHz A-line acquisition rate) normalized to the reference axial resolution obtained from curve 0 (circles, black). The resolution obtained from the simulated A-line profiles is also shown (red line). Up to a 6-fold degradation of the axial resolution was observed both in the experimental and simulation results. Harmonic distortion in the speaker motion may account

#3980 - $15.00 US
Received 5 March 2004; revised 17 June 2004; accepted 21 June 2004

for the discrepancy between the two results. Figure 15(b), plotted on a different vertical scale, shows a similar plot of the measured and calculated axial resolution for an A-line acquisition rate of 16 kHz. The 16 A-lines were again extracted with uniform time interval during a single oscillation of the sample mirror. The maximum broadening in this case was less than a factor of 1.3, highlighting the importance of rapid acquisition for minimizing resolution degradation.

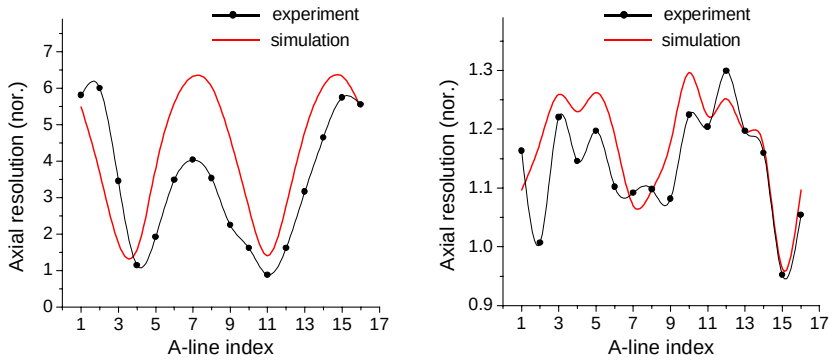

Fig. 15. (a) Normalized axial resolution obtained at an A-line rate of 2 kHz, normalized to the unperturbed resolution obtained with a stationary mirror. (b) Normalized axial resolution obtained at an A-line rate of 16 kHz. Black circles: measured values. Red line: simulation.

3.2.3 Transverse scanning

The effect of transverse motion was also investigated by using a similar experimental method as described in Section 2.2.3. A 90-degree, BK7 prism was mounted so that the probe beam could be scanned across the apex between the orthogonal faces (depicted in Fig. 11). To increase diffuse scattering of the probe beam from the prism, its surfaces were roughened using a polishing film with a 15 μm grain size. In this experiment, the galvanometer was driven with a saw-tooth waveform at a frequency of approximately 30 Hz in synchrony with the A-line acquisition. A total of 520 A-lines were acquired at a rate of 15.7 kHz during each scan of the galvanometer (33 ms). To obtain various scan speeds of the probe, we changed the peak-to-peak amplitude of the applied voltage from 0 to 20 V. At amplitudes greater than 5 V, the transverse scan distance was limited by the maximum angular range of the galvanometer and the finite size of the lens. However, the scan velocity in the middle of the scan range, near the neutral position of the galvanometer, was approximately linearly proportional to the voltage swing with a coefficient of ~114 mm/s/V.

Figure 16 shows typical images of the prism obtained at different transverse scanning velocities (denoted by the galvanometer drive voltage amplitude). The images were plotted using a logarithmic inverse grayscale over a dynamic range of 30 dB in reflectivity. The scale bars represent 1.0 mm. The transverse displacement of the probe beam between adjacent A-lines is proportional to the voltage with a coefficient of ~7.6 μm/V. Therefore, the images obtained at higher driving voltages consist of fewer numbers of A-lines. The image obtained at 20 V exhibits significant blurring in both the axial and transverse directions. The 90-degree apex angle in the images confirms that the transverse motion does not cause the Doppler frequency shift as observed with axial motion. We note that the depth change in the image as a result of transverse beam scanning over a slanted structure should not be confused by the axial motion of the sample described earlier. An important distinction is that for transverse scanning the phase of the interference signal from each scatter is invariant during A-line acquisition whereas it is chirped when either the sample or the probe is in an axial motion.

#3980 - $15.00 US
Received 5 March 2004; revised 17 June 2004; accepted 21 June 2004

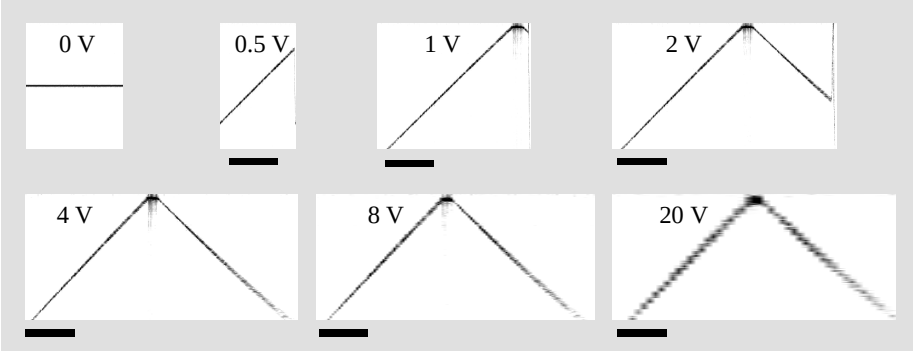

Fig. 16. OFDI images of a prism at various amplitudes of the galvanometer scan voltage. With increasing amplitude, the scan velocity is increased and therefore the image contains a fewer number of A-line. The

To compare the measurements of Fig. 16 with the theory of section 3.1.3, the signal power and FWHM of 10 A-lines at the slope of the prism near the center of the images were analyzed. Due to speckle, the 10 A-line profiles in each image had variations in signal peak power with a standard deviation of +/- 3 dB. Figure 17(a) depicts the mean of the 10 measured values (squares) for each image, as a function of the normalized displacement between adjacent A-lines. The experimental results were fit reasonably well with a theoretical curve based on Eq. (26) with α = ~0.4. (red line, Fig. 17a).

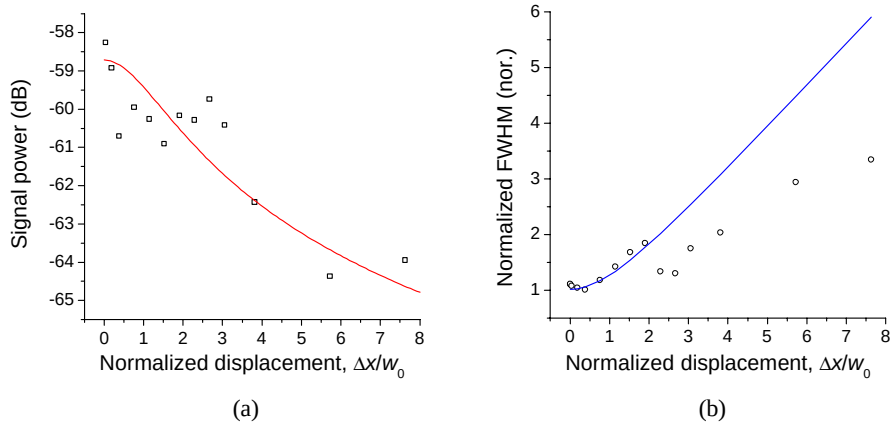

(a) (b)

Fig. 17. (a) Signal peak power (squares, black) measured from the average of 10 A-line profiles for each normalized displacement. Red line: theorical curve for speckle-averaged signal power with α = 0.4 in Eq. (26). (b) Normalized minimum FWHM of the image (circles, black) obtained from 10 A-line profiles. Theorical curve of axial resolution assuming a single scatter sample (line, blue).

Equation 25 predicts the broadening of intrinsic axial resolution due to transverse motion. Unlike a mirror, the FWHM of an A-line profile of a scattering sample is affected by the speckle. In the presence of transverse sample motion or beam scanning, the FWHM can be broadened significantly simply because the depth of the scattering points being illuminated is changed during an A-line acquisition time. The magnitude of this broadening effect should be sensitive to the scatterer distribution and size in the sample. The measured FWHM values from the image in Fig. 16 showed large variations due to speckle. Figure 17(b) shows the minimum values of FWHM (circles) taken from each set of 10 A-lines, normalized to the

#3980 - $15.00 US
Received 5 March 2004; revised 17 June 2004; accepted 21 June 2004

FWHM measured with the transverse scanning galvanometer held fixed (0 V). The theoretical curve based on Eq. 25 (blue line, Fig. 17b) agrees reasonably well with the experimental values. However, the theory overestimates the FWHM values, which we attribute to relatively large scatterer sizes instead of the point scatters assumed in the theory. For a given motion velocity, higher A-line acquisition rates are desired to avoid degradation of image quality.

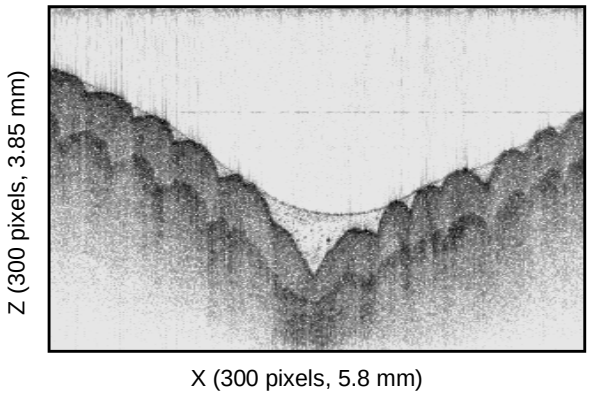

Fig. 18. OFDI image of a human finger near skin fold (300 axial x 300 transverse pixels, 3.8 mm x 5.8 mm) acquired with the OFDI system at an A-line rate of 15.7 kHz.

To test OFDI for a biological sample, we imaged the ventral portion of a volunteer's finger near a skin fold. Figure 18 depicts the image (300 axial × 300 transverse pixels) acquired at an A-line acquisition rate of 15.7 kHz. The focal point of the imaging lens was positioned in the middle of the depth range. The vertical axis extends over a depth of 3.8 mm. The horizontal axis extends over a distance of 5.8 mm. The transverse displacement during single A-line acquisition time was approximately 18 μm for duty cycle of 94% of the system. This corresponds to $\Delta x/w_0 = 1$. At this low value, as expected from previous results in Fig. 17, negligible degradation in spatial resolution and SNR was observed in the tissue image. The skin fold region is seen as sharp as other areas despite the fact that the depth change between adjacent A-lines corresponds to several hundreds of optical wavelength.

3.3 Discussion

We have shown that axial motion can give rise to several artifacts in OFDI images: Doppler-induced depth error, reduction in spatial resolution, and SNR degradation. Transverse sample motion or beam scanning can also cause degradation in spatial resolution and, to some extent, SNR.

The Doppler shift is proportional to axial motion velocity. If the sample is under rigid motion, the Doppler shift would be uniform throughout the whole image. This causes merely a shift of the whole image and does not necessarily degrade the image quality. However, if the axial velocity is a function of location in the sample, the Doppler shift leads to spatial image distortion. If the Doppler-induced depth error can be tolerated up to M times the axial resolution, the maximum allowable axial displacement would be given, using Eq. (20), by $\Delta z_{\max} = (0.44/\sigma) M \lambda$. For M = 10, σ = 0.71, λ = 1.3 μm, we get $\Delta z_{\max}$ = 8 μm. This corresponds to a velocity of 130 mm/s for T = 62.5 μs (A-line rate of 16 kHz) or 16.3 mm/s for T = 500 μs (A-line rate of 2 kHz).

The degradation in spatial resolution causes blurring of images. Equation (21) predicts the degradation of axial resolution in the case of linear tuning in k-space. If the resolution broadening can be tolerated up to a factor of M', we obtain $\Delta z_{\max} = \delta z_0 (M'^2 - 1)^{1/2} / (2\sigma)$.

#3980 - $15.00 US Received 5 March 2004; revised 17 June 2004; accepted 21 June 2004

For $M' = 2$, $\sigma = 0.71$, and $\delta z_0 = 10$ μm, we obtain $\Delta z_{max} = 12.2$ μm, which corresponds to a velocity of 195 mm/s for $T = 62.5$ μs or 24.4 mm/s for $T = 500$ μs. Motions that might occur in medical imaging *in vivo* may have a velocity range less than 100 mm/s. Therefore, we expect that the Doppler distortion and image blurring may be negligible for high A-line acquisition rate beyond 10 kHz. However, for a slow acquisition rate, the motion effects may need to be taken into account.

Equation (25) describes the broadening of spatial resolution by transverse motion. If the broadening can be tolerated up to a factor M'', the maximum allowable transverse displacement is given by $\Delta x_{max} = w_0 (M''^2 - 1)^{1/2} / \sigma$. For $M'' = 1.41$, $\sigma = 0.71$, $w_0 = 18$ μm, we obtain $\Delta x_{max} = 25$ μm. This corresponds to 400 mm/s in velocity for $T = 62.5$ μs. For an application using a rotating fiber-optic catheter [30], the radius-circumferential image will be blurred more at large radius along both radial and circumferential directions. A maximum allowable amount of blurring puts a limit on the minimum number of A-lines to be acquired per image (one revolution of the catheter) as $A_{min} = 2\pi R / \Delta x_{max}$, where R is the ranging depth (radius). For example, for $R = 4$ mm and $\Delta x_{max} < 25$ μm, a minimum 1000 A-lines needs to be acquired per one revolution of the catheter.

4. Summary

In conventional OCT using time domain ranging, the motion at a given time will affect only the particular image pixel that is being acquired. Since the acquisition time of each pixel is typically only a few microseconds in most medical imaging, the degradation of SNR and spatial resolution of each pixel may be negligible. Instead, the motion may result in image distortion owing to non-uniform space sampling. In OCT using frequency domain ranging, however, the effect of motion tends to be more serious and complicated because the signal is integrated over time as in SD-OCT and the image is obtained by the Fourier transform integration. We have described the theory and experimental verifications of various motion artifacts in two interferometric methods: SD-OCT and OFDI.

An important parameter governing the magnitude of motion artifacts is the normalized displacement, defined as the total axial or transverse displacement during a single A-line signal acquisition time. For a given sample motion, as the A-line rate is increased, the axial and transverse displacements are decreased and so are the motion artifacts. We have discussed the implications of the motion artifacts in clinical applications and emphasized the benefit of fast A-line acquisition time. On the other hand, the motion artifacts arising from the transverse scanning of the probe beam is not necessarily mitigated by a faster A-line rate if the beam scanning speed is to be increased commensurate with the increased A-line rate. A faster A-line rate, however, may allow a larger number of A-lines to be acquired per frame to reduce the beam displacement between adjacent A-lines.

The analysis and results presented here may be useful for the design of biomedical imaging systems as well as for the development of methods to avoid or mitigate the motion artifacts.

Acknowledgment

This research was supported in part by the National Institutes of Health contracts R01-HL70039 and R01-RR019768, the Center for Integration of Medicine and Innovative Technology (for technical development only), and by a generous gift from Dr. and Mrs. J. S. Chen to the optical diagnostics program of the Massachusetts General Hospital Wellman Center of Photomedicine.

#3980 - $15.00 US Received 5 March 2004; revised 17 June 2004; accepted 21 June 2004